Supporting Information

Electronic delocalization in the radical cations of porphyrin oligomer molecular wires

Martin D. Peeks,[†,§] Claudia E. Tait,[‡,§] Patrik Neuhaus,[†] Georg M. Fischer,[†] Markus Hoffmann,[†] Renée Haver,[†] Arjen Cnossen,[†] Jeffrey R. Harmer,[‡] Christiane R. Timmel,[*,‡] and Harry L. Anderson[*,†]

[†]Chemistry Research Laboratory, University of Oxford, 12 Mansfield Road, Oxford, OX1 3TA, United Kingdom

[‡]Centre for Advanced Electron Spin Resonance, University of Oxford, Oxford, OX1 3QR, United Kingdom

[§]These authors contributed equally

Table of Contents

Materials

The zinc porphyrin oligomers (***l*-P1** to ***l*-P6**, ***c*-P6**, ***c*-P6·T6** and ***t*-P12·(T6)$_2$**) depicted in Figure 1 of the main text were synthesized according to previously published procedurea.[1–3] All manipulations of air- or water-sensitive compounds were performed using standard high-vacuum techniques. Commercially available reagents were used without further purification unless otherwise noted. Tris(4-bromophenyl)ammoniumyl hexachloroantimonate (BAHA) was purchased from Fluka. Thianthrenium hexachloroantimonate (THA) was prepared according to reference [4]. Dry THF, CH_2Cl_2, and toluene were obtained by passage of the solvent through alumina under N_2 pressure. CH_2Cl_2 for spectroelectrochemistry was purchased unstabilized (Fisher), and purified by washing with conc. H_2SO_4, then water, then distillation from CaH_2 and storage over activated 4 Å molecular sieves.

Samples for the EPR measurements were prepared in d_8-toluene:d_8-THF:CD_2Cl_2 1:1:1 and degassed using several freeze-pump-thaw cycles. The oxidant (as a solution in CD_2Cl_2) was added under Ar atmosphere just before the EPR measurements. For the low-temperature measurements the samples were then frozen in liquid nitrogen. For W-band measurements, an aliquot of sample was transferred from an X-band tube (3.8 mm o.d.) to the W-band tube (0.9 mm o.d.) by syringe.

Chemical Oxidation

For redox titrations, one equivalent of BAHA (0.5 mM in CH_2Cl_2) was added to a solution of porphyrin oligomer (~1 μM in CH_2Cl_2) in four steps. To check the reversibility of the oxidation, an excess of ferrocene was added. The discontinuity in absorption at 860 nm is due to an instrumental inaccuracy at a grid changeover. The results are shown in Figure S8.

Spectroelectrochemistry

Experimental details. Spectroelectrochemical (SEC) experiments were performed in an optically transparent thin layer electrochemistry (OTTLE) cell comprising platinum gauze working and counter electrodes and a Ag/AgCl quasireference electrode.[5] This OTTLE cell was purchased from Prof. Frantisek Hartl, University of Reading, UK. The electrolyte solution was 0.1 M tetra-*n*-butylammonium hexafluorophosphate (Bu_4NPF_6 or TBAP) in CH_2Cl_2. Optical data were collected using a Bruker Vertex 80 FT-IR spectrometer with a HeNe laser probe. The optical path was purged with dry N_2. Vis spectra were collected with a UV-CaF_2 beamsplitter, tungsten source and RT-Si diode detector; NIR spectra with a CaF_2 beamsplitter, tungsten source and RT-DLaTGS detector, and IR spectra with a KBr beamsplitter, Globar source and LN_2-MCT detector. Spectra were collected every ~1.2 s whilst a cyclic voltammetry (CV) experiment was performed in the OTTLE cell. A slow scan rate (5 mV s^{-1}) was used for the CV to promote equilibrium conditions for each potential step. The SEC data were symmetric about the upper vertex potential of the CV, revealing the reversibility of oxidation. The upper vertex was adjusted to the *N*+ oxidation state of each oligomer, since oxidation into the 2*N*+ band[6] resulted in irreversibility at room temperature.

Curve fitting. The raw SEC data from each wavelength range (vis, NIR and IR, Figure S1) were trimmed to remove noisy data on the edge of each region and to contain only the anodic sweep of the CV (Figure S2). For each oligomer, the wavelength ranges were merged to give a single matrix of spectral data (Figure S3, for ***l*-P3**). Unsubtracted solvent signals in the IR/NIR regions were removed by subtraction of the early-time spectra from the entire data matrix: formally, the IR/NIR regions are therefore difference spectra, but since the IR bands in the neutral oligomers are extremely weak (Figure 8), the subtraction process has no impact on the overall results. The components describing the spectral data, and their speciation curves, were extracted by multivariate curve resolution employing

the MCR-ALS toolkit in MATLAB.[7,8] For ***l*-P6**, only five components could be resolved: the neutral, 1+, 3+, 5+ and 6+ oxidation states, due to near degeneracy with adjacent states of the 2+ and 4+ states. Similarly, only seven components could be resolved for ***t*-P12·(T6)$_2$**. For ***l*-P4**, the curve resolution was improved by fitting with six components (as opposed to the expected five components), since the algorithm provided unphysical spectra when five components were used. The additional component appeared between the neutral and 1+ oxidation states, and is considered artefactual (and thus omitted from Figures 3 and S4) because (a) it has essentially the same absorption spectrum as the neutral oxidation state and (b) it appears before any charge transfer is observed in the cyclic voltammetry experiment. In this paper, we have focused discussion on the 1+ and, briefly, *N*+ oxidation state of each oligomer, since we cannot exclude the presence of significant rotational ambiguity in the other oxidation states of longer oligomers (***l*-P5**, ***l*-P6**, ***c*-P6**, and ***t*-P12·(T6)$_2$**, excluding ***c*-P6·T6**, in which all seven oxidation states can be confidently resolved).

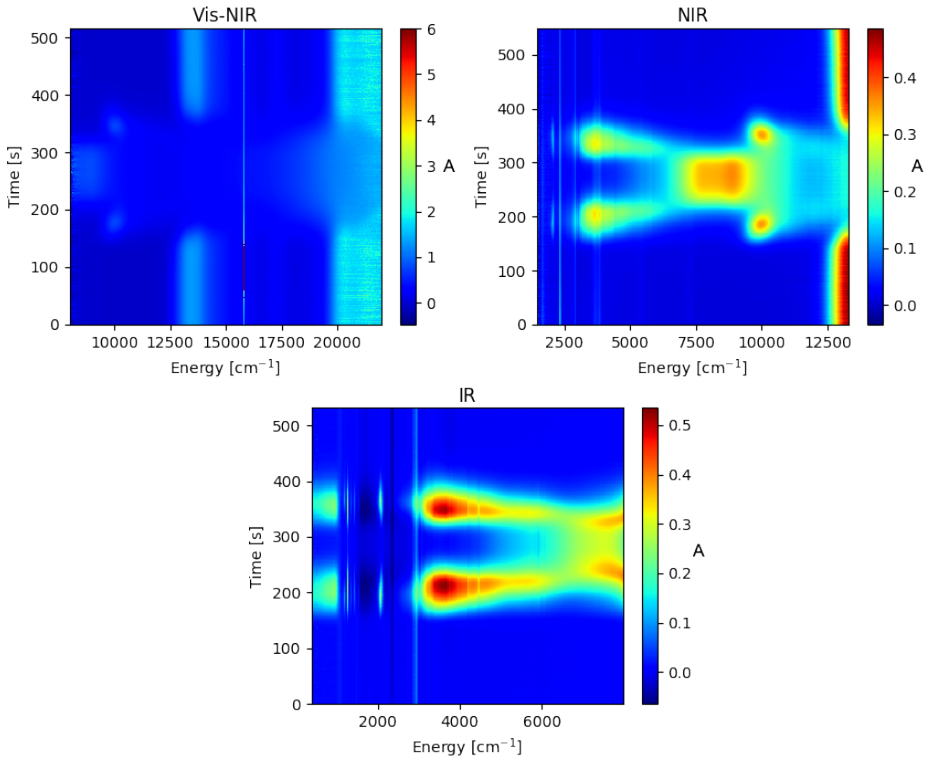

Figure S1. Raw spectroelectrochemical data for ***l*-P3**, measured in CH_2Cl_2/0.1 M Bu_4NPF_6 at room temperature.

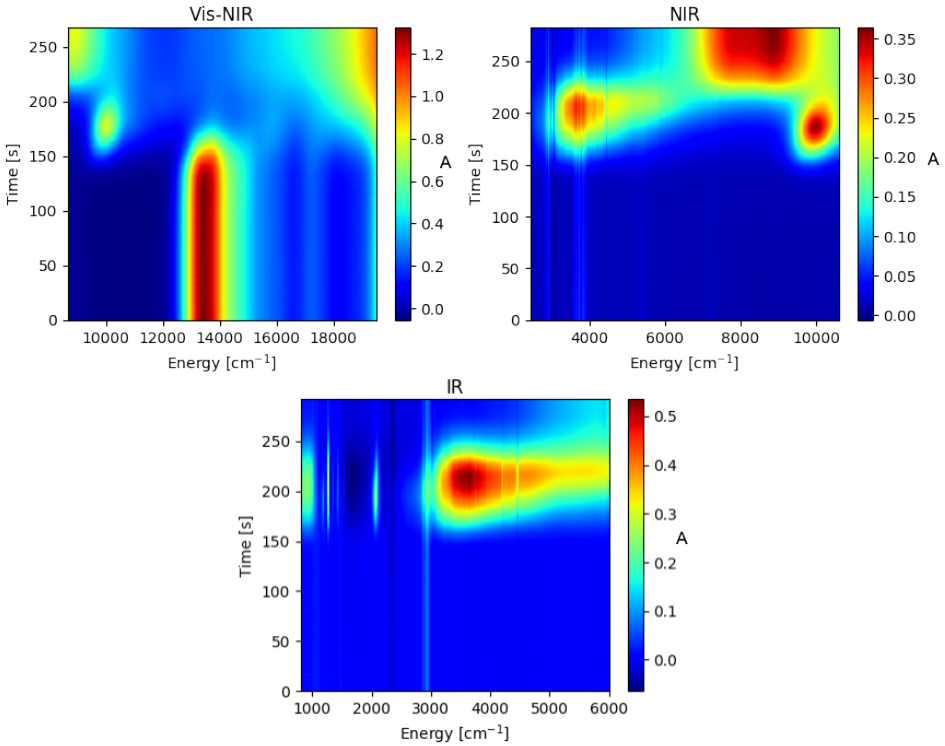

Figure S2. Spectroelectrochemical data for ***I*-P3** from Figure S1 after removal of noisy edges and truncation of the time axis to show only the anodic (oxidation) sweep of the cyclic voltammograms.

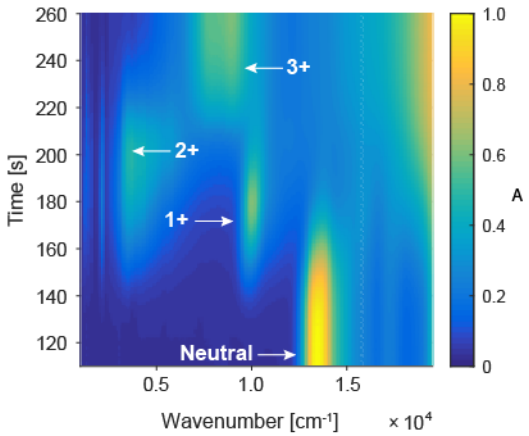

Figure S3. Merged spectroelectrochemical data for ***I*-P3**, revealing four clearly identifiable distinct component spectra, shown with white arrows.

Table S1. Fit parameters for the Meier plots in main text Figure 6

Band	$\nu_{max}(1)$ (cm^{-1})	$\nu_{max}(\infty)$ (cm^{-1})	α	R^2
P_1	5353 ± 2118	3410 ± 86	1.4 ± 1.1	0.75
P_2	12531 ± 261	9732 ± 15	1.2 ± 0.1	0.9969
C≡C str.	2182 ± 60	2056 ± 1	1.7 ± 0.5	0.9728

Table S2. Calculations of N_{deloc} from extinction coefficients and oscillator strengths (f) of the P_2 and Q bands for porphyrin oligomer radical cations.

	ε_Q[†]	ε_2[†]	N_{deloc}[‡]	f_Q	f_2	N_{deloc}[¶]
***l*-P2$^{+\bullet}$**	0.22	0.93	1.62	0.05	0.37	2.00
***l*-P3$^{+\bullet}$**	0.52	1.27	2.13	0.19	0.61	2.50
***l*-P4$^{+\bullet}$**	0.77	1.21	2.44	0.39	0.50	2.53
***l*-P5$^{+\bullet}$**	1.40	1.41	2.51	0.86	0.68	2.40
***l*-P6$^{+\bullet}$**	1.90	1.24	2.37	1.34	0.69	2.20

[†] Units $M^{-1}cm^{-1}$ ($\times 10^{-5}$); [‡] determined according to main text equation 2;

[¶] determined according to main text equation 3.

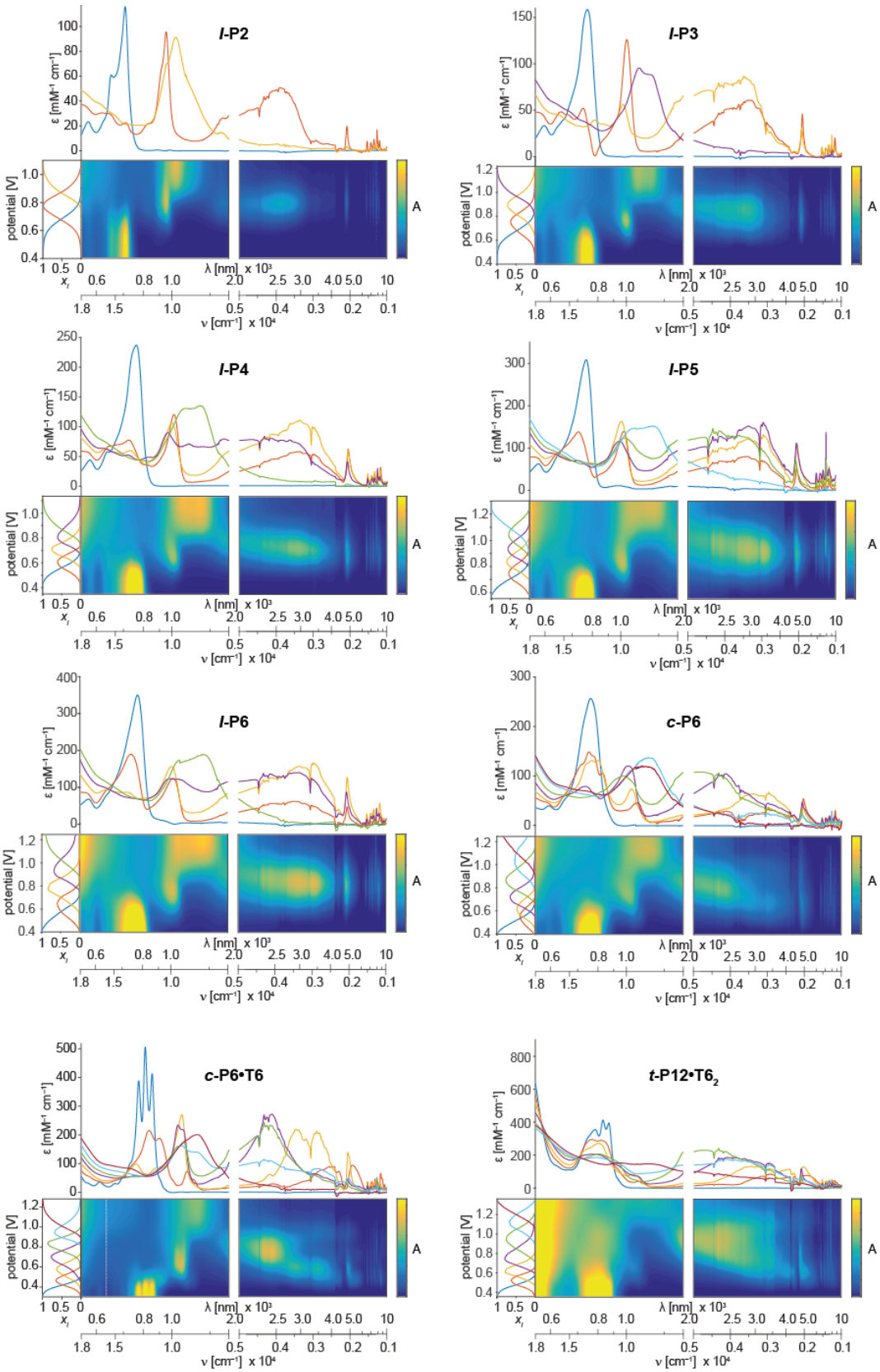

Figure S4. Resolved spectra for porphyrin oligomer oxidation states from spectroelectrochemistry, in CH_2Cl_2 with 0.1 M Bu_4NPF_6. The surface plots show the pre-processed spectral data, with a normalized absorption (color) axis. Above each surface plot is the series of extracted spectra, with the corresponding speciation profiles shown to the left. The color with which each spectrum is drawn corresponds to the color of the related curve in the speciation plot.

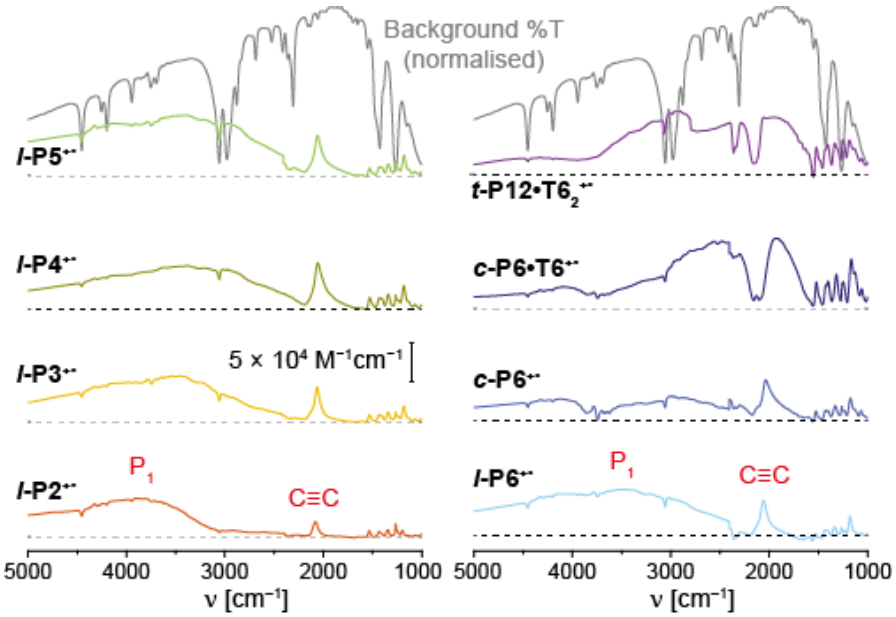

Figure S5. Plots of the IR spectra for porphyrin oligomer radical cations from spectroelectrochemistry in CH_2Cl_2 / 0.1 M Bu_4NPF_6. The background transmission spectrum is shown in gray at the top of the figure.

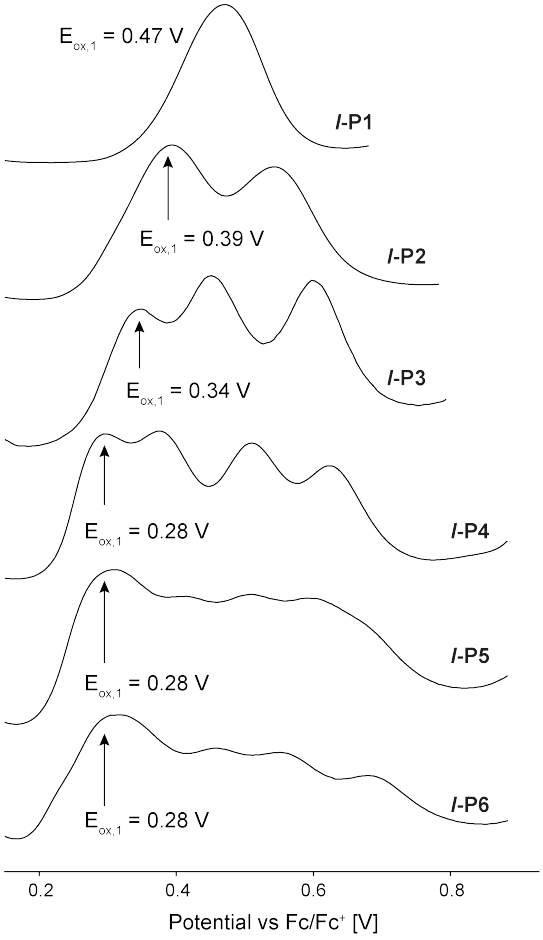

Figure S6. Experimental square wave voltammetry (CH_2Cl_2/0.1 M Bu_4NPF_6) of porphyrin oligomers. Glassy carbon working electrode; platinum wire counter electrode and Ag/AgCl reference electrode. Fc/Fc^+ was used as an internal reference. 5 mV step potential, 10–50 mV modulation amplitude, 5 Hz frequency. The voltammograms are cropped to show only the first oxidation manifold (up to 1+ charge per porphyrin unit). The voltammetric data for ***l*-P1** and ***l*-P2** were reported previously.[6]

UV-vis, IR and Raman spectroscopy

For non-spectroelectrochemical measurements, UV-Vis absorption spectra were recorded at ambient temperature with a Perkin–Elmer Lambda 20 or a Perkin–Elmer Lambda 1050 spectrometer using Infrasil cuvettes (1 cm pathlength, 3 mL, Starna). IR spectra were recorded using a Bruker Tensor 27 (RT-DLaTGS detector) in a solution cell with KBr windows. Raman spectra were recorded using a Bruker MultiRAM FT-Raman spectrometer with a 1064 nm Raman probe, resonant with the cation absorption P_2 band of ***c*-P6·T6$^{+\bullet}$**.

Absorption spectra of neutral oligomers

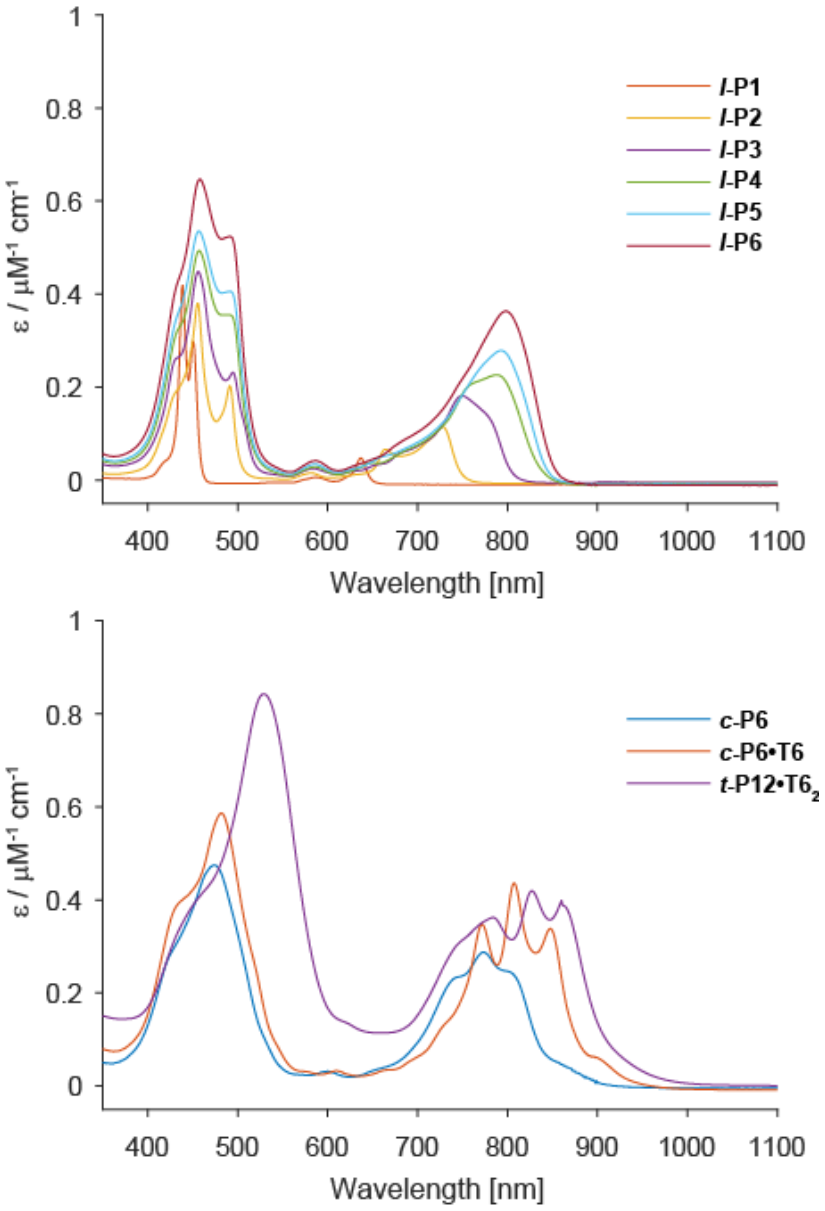

Figure S7. Absorption of the linear and cyclic porphyrin oligomers CH_2Cl_2:THF 10:1 at room temperature.

Absorption spectra of radical cations generated by chemical oxidation

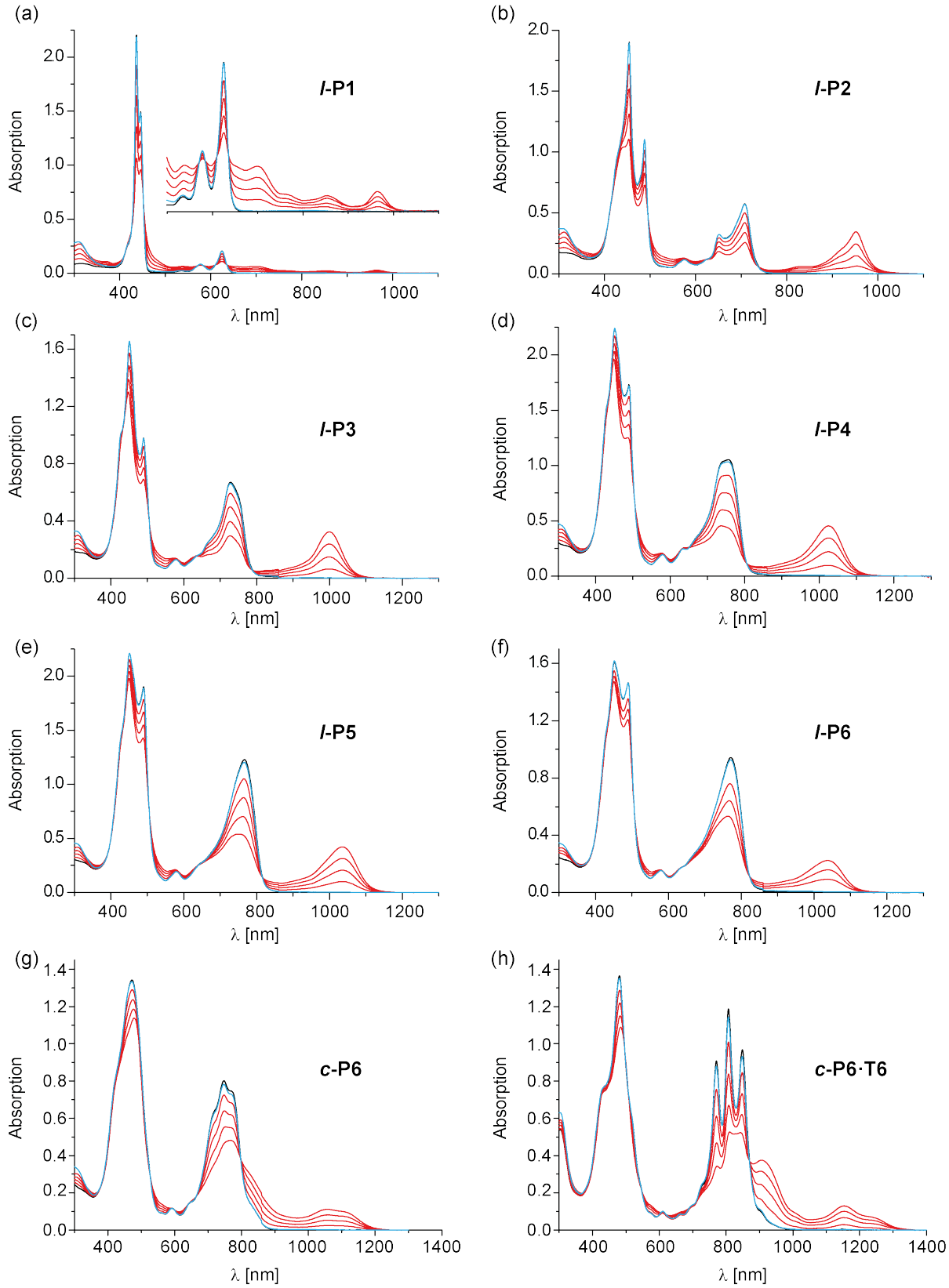

Figure S8. Titration of ***l*-P1** to ***l*-P6, *c*-P6·T6** and ***c*-P6** in CH_2Cl_2 with BAHA: neutral = black, oxidation = red and reduction with ferrocene = blue.

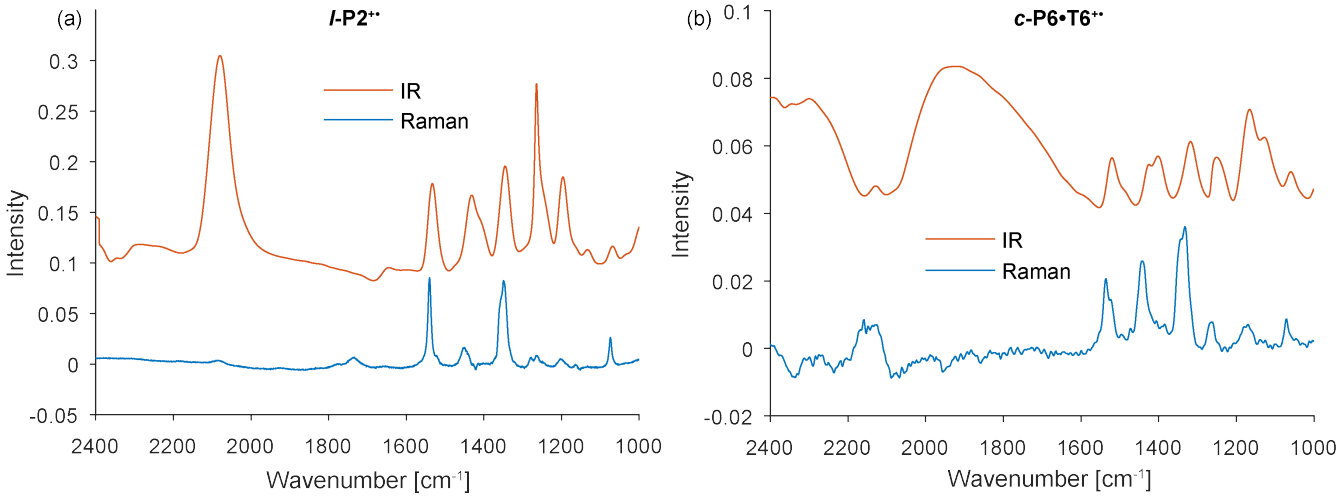

Figure S9. Comparison of solution Raman (CH_2Cl_2, oxidation with BAHA) and SEC IR spectra of ***l*-P2**$^{+\bullet}$ (a) and ***c*-P6·T6**$^{+\bullet}$ (b). For (a) the Raman probe was at 830 nm; for (b) it was at 1064 nm. In both cases the Raman probes were resonant with the cation P_2 band. The Raman samples were prepared by chemical oxidation, and by UV-vis spectroscopy appeared to be a mixture of monocation and neutral oxidation states.

Continuous wave EPR

Continuous wave (cw) X-band EPR measurements were performed at room temperature and at 100 K on a Bruker Biospin GmbH EMX spectrometer equipped with a high sensitivity Bruker probe head and an Oxford Instruments helium-flow cryostat. EPR spectra were recorded at a microwave frequency of *ca.* 9.40 GHz with modulation amplitudes and frequencies of 0.01 mT and 100 kHz, respectively. The microwave power was adjusted in order to avoid spectral distortions. EPR experiments on samples with different radical cation concentrations were performed and no concentration-dependence of the linewidth or lineshape was detected.

Table S3. Peak-to-peak linewidth determined through Gaussian fitting of the experimental room temperature EPR spectra (see Figure 9 or Figure S11) and number *N* of molecular sites the electron spin is delocalized over calculated using equation 4 from the main text.

	ΔB_{pp} [mT]	*N*
***l*-P1**$^{+\bullet}$	0.5697 ± 0.0161	1.0 ± 0.1
***l*-P2**$^{+\bullet}$	0.3917 ± 6E-04	2.1 ± 0.1
***l*-P3**$^{+\bullet}$	0.3424 ± 2E-04	2.8 ± 0.2
***l*-P4**$^{+\bullet}$	0.2992 ± 1E-04	3.6 ± 0.2
***l*-P5**$^{+\bullet}$	0.2604 ± 1E-04	4.8 ± 0.3
***l*-P6**$^{+\bullet}$	0.2370 ± 1E-04	5.8 ± 0.3
***c*-P6**$^{+\bullet}$	0.2294 ± 1E-04	6.2 ± 0.3
***c*-P6·T6**$^{+\bullet}$	0.2742 ± 1E-04	4.3 ± 0.2
***t*-P12·(T6)$_2$**$^{+\bullet}$	0.1795 ± 3E-04	10.1 ± 0.6

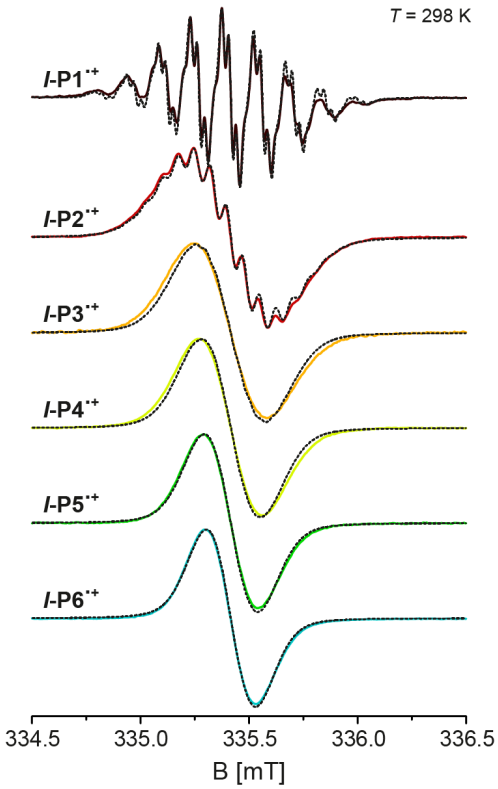

Figure S10. Comparison of the experimental and simulated room temperature EPR spectra of the radical cations of ***l*-P1** to ***l*-P6**. Simulations were performed in EasySpin[9] with the following parameters for ***l*-P1**: four equivalent nitrogen nuclei with an isotropic hyperfine coupling of 4.05 MHz and four equivalent protons with a hyperfine coupling of 0.90 MHz. For the longer oligomers the number of nuclei was increased depending on *N* and the hyperfine couplings were scaled accordingly.

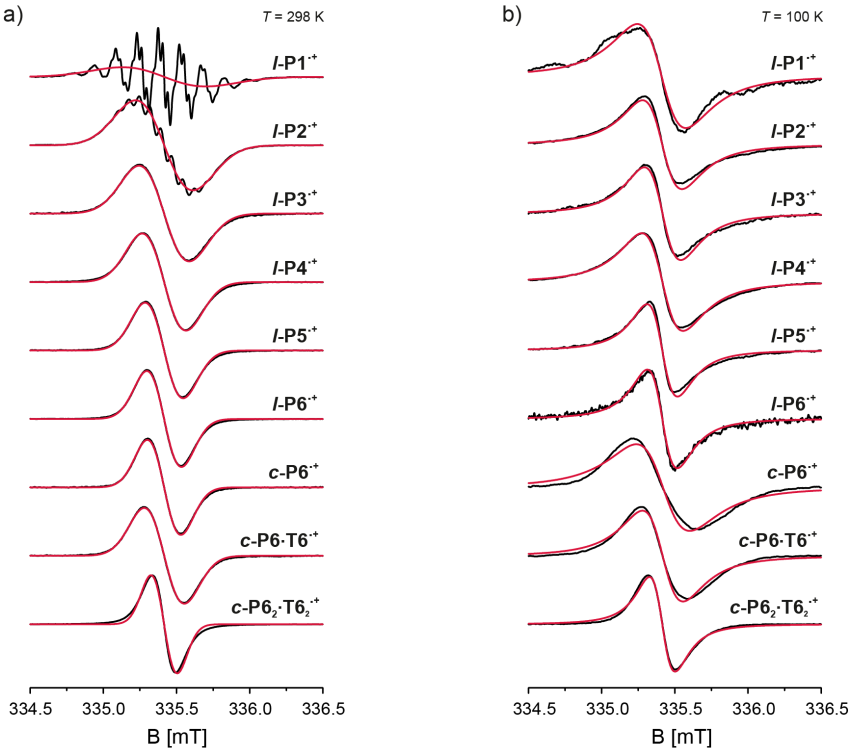

Figure S11. Experimental room temperature (a) and 100 K (b) X-band cw-EPR spectra (black) of the radical cations of ***l*-P1** to ***l*-P6**, ***c*-P6**, ***c*-P6·T6** and ***t*-P12·(T6)$_2$** and fitted derivative Gaussian (a) and Lorentzian (b) functions (red).

Pulse EPR

Pulsed EPR measurements were performed on a X-/W-band Bruker Elexsys 680 spectrometer equipped with helium gas-flow cryostats from Oxford instruments.

^{1}H Mims ENDOR spectra were recorded with the pulse sequence $\frac{\pi}{2} - \tau - \frac{\pi}{2} - T - \frac{\pi}{2} - \tau - echo$ with mw pulse lengths of $t_{\pi/2}$= 44 ns, τ = 200 ns and a radiofrequency pulse length of 18 µs; the RF power was adjusted to form a π pulse. The ENDOR spectra were recorded at the magnetic field corresponding to the echo maximum and *ca*. +1 mT from the echo maximum for the linear oligomers, −1 mT for ***c*-P6** and −0.8 mT for ***c*-P6·T6** to investigate orientational selectivity. Mims ENDOR spectra recorded with a 100 µs radiofrequency π pulse only showed negligible differences limited to the central region of the ENDOR spectrum confirming the absence of power broadening. Mims ENDOR spectra recorded with different τ values and ENDOR spectra recorded with the Davies ENDOR pulse sequence, $\pi - T - \frac{\pi}{2} - \tau - \pi - \tau - echo$, with mw pulse lengths of $t_{\pi/2}$ = 100 ns, t_π = 200 ns and *T* = 20 µs, τ = 200 ns and a radiofrequency pulse length of 18 µs, were compared in order to rule out the presence of any distortions due to blind spots in the recorded spectra. No temperature-dependence of the ENDOR spectra was detected in the range from 6 to 100 K. We were unable to perform ENDOR experiments above the freezing point of the solvent mixture.

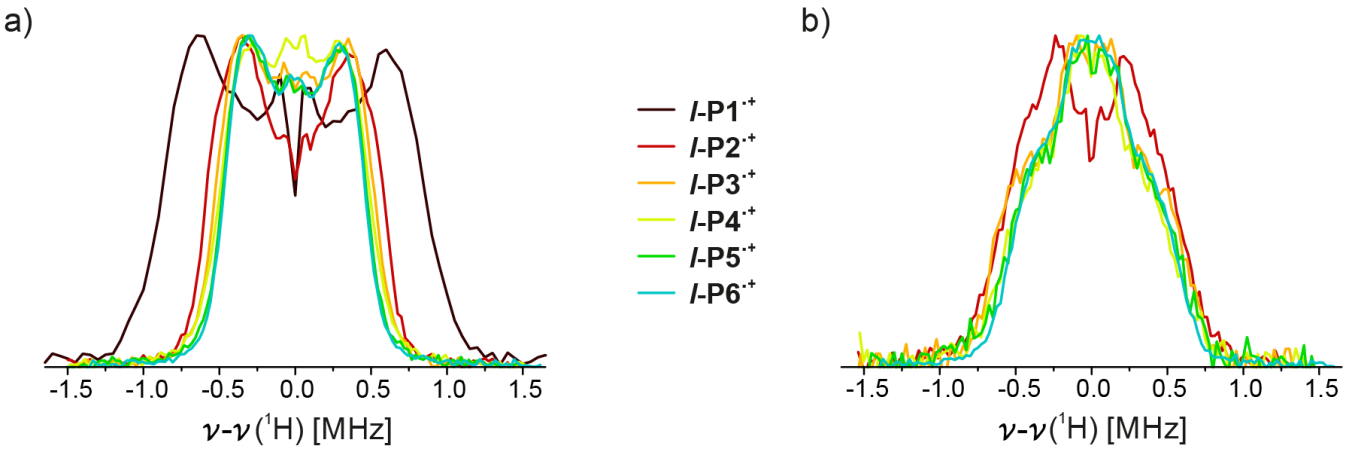

Figure S12. W-band ^{1}H Mims ENDOR spectra of the radical cations of the linear oligomers ***l*-P1** to ***l*-P6**, generated by oxidation with THA, in d_8-toluene:d_8-THF:CD_2Cl_2 1:1:1 recorded at 80 K at the field positions corresponding to $g_\perp$ (a) and to $g_\parallel$ (b).

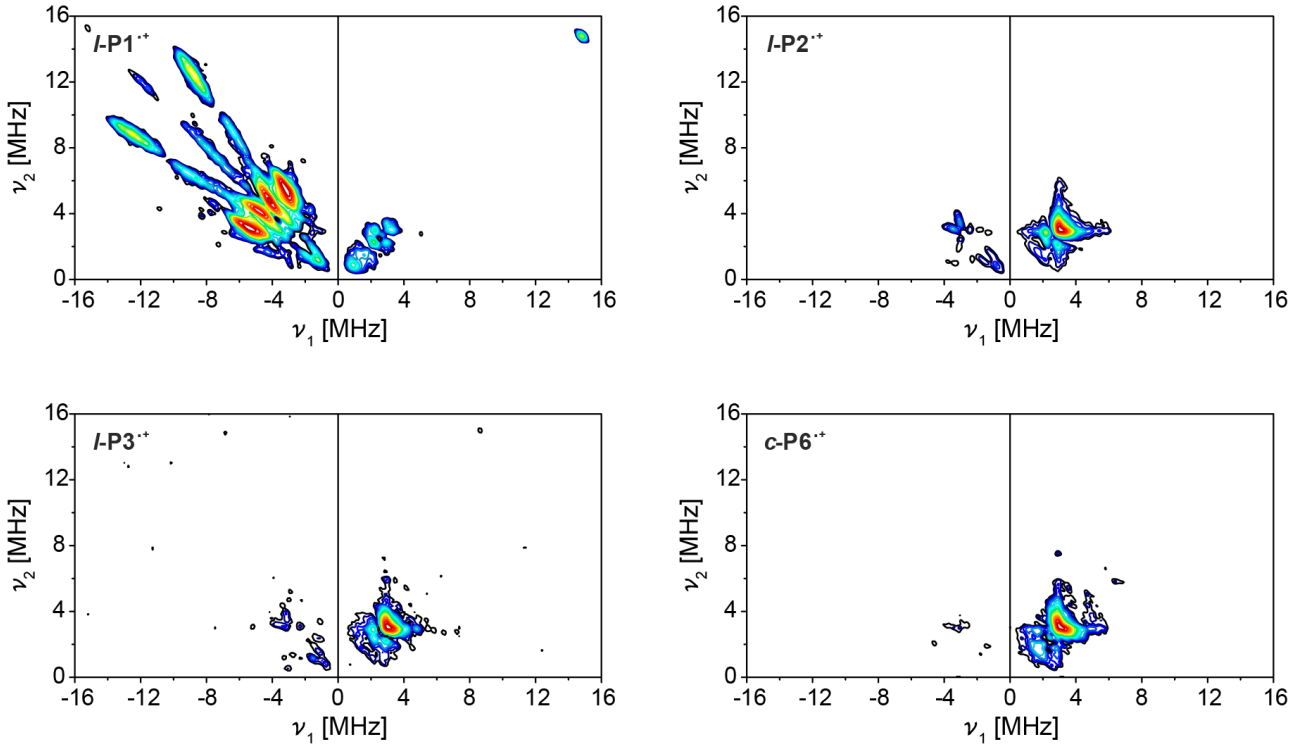

Figure S13. X-band ^{14}N HYSCORE spectra of the radical cations of ***l*-P1**, ***l*-P2**, ***l*-P3** and ***c*-P6** generated by oxidation with THA, in deuterated toluene:THF:CD_2Cl_2 1:1:1 recorded at 80 K.

Calculation of spin densities, TD-DFT, IR and Raman

Gaussian09/D.01 was used for all calculations in this section,[10] with the 6-31G* basis set.[11–14] Aryl side-groups and acetylene protected groups were all truncated to -H and geometry optimizations were initiated in the maximum possible symmetry (typically D_{2h} for linear oligomers). The self-interaction error in DFT can cause a dramatic overestimation of charge and spin delocalization, but with the choice of an appropriate functional, significant error can be avoided. We thus compared the ability of different functionals to reproduce, using TD-DFT, the position of the P_1 band for the radical cations of ***l*-P2**, ***l*-P4** and ***l*-P6**. We tested B3LYP,[15] ωB97X-D,[16] and LC-ωPBE (with ω = 0.1 a_0^{-1} and ω = 0.2 a_0^{-1}).[17] The CH_2Cl_2 PCM solvent model was used. The test functionals were used for both geometry optimizations (gas phase) and TD-DFT calculations (PCM model), and the stationary nature of the converged geometries were all confirmed by frequency calculations (no imaginary frequencies). As expected, B3LYP significantly overestimated the extent of delocalization, showing a significant progressive red-shift of P_2 upon oligomer homologation (Figure S14). LC-ωPBE (ω = 0.1 a_0^{-1}) similarly overestimated charge delocalization. In contrast, both LC-ωPBE (ω = 0.2 a_0^{-1}) and ωB97X-D fit the experimental data excellently (Figure S14). It is worth noting the range separation parameter ω for ωB97X-D is also 0.2 a_0^{-1}. In their studies on monoalkyne-linked porphyrin oligomers, Therien and coworkers employed LC-ωPBE (ω = 0.05 a_0^{-1}).[18] After this parameterization, we used LC-ωPBE (ω = 0.2 a_0^{-1}) for TD-DFT and IR calculations shown in Figures S17 and S10, respectively. IR frequencies were scaled by a factor of 0.951, as appropriate for HSEh1PBE.[19] Cartesian coordinates are provided as text files in a supporting .ZIP file.

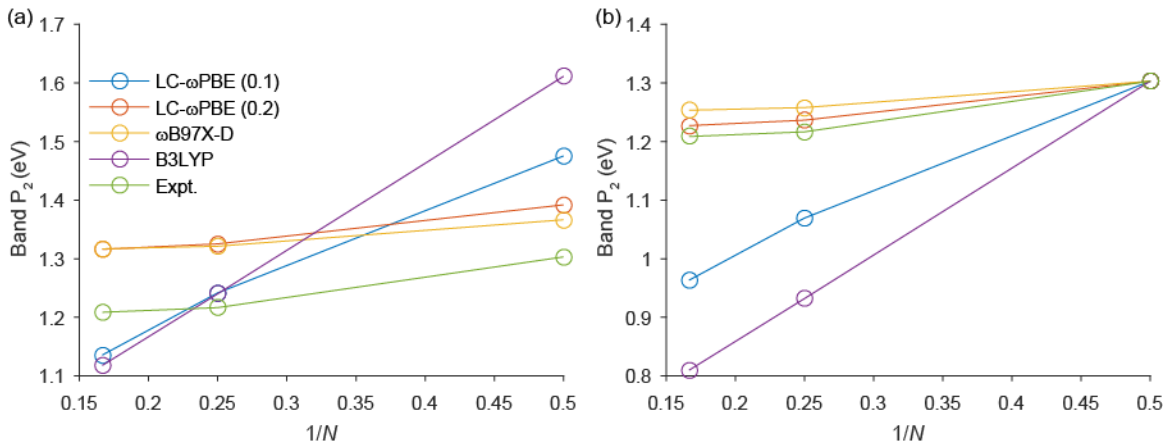

Figure S14. Comparison of calculated excitation energies for the P_2 band compared to experiment for ***I*-P2$^{+\bullet}$**, ***I*-P4$^{+\bullet}$** and ***I*-P6$^{+\bullet}$**. In (b), an equal energy offset has been subtracted for the results from each functional, such that the excitation energy for ***I*-P2$^{+\bullet}$** is equal to experiment. Lines are a guide to the eye.

Charge and spin populations were calculated using the Natural Population Analysis (NPA) method implemented in NBO6, using the same density as for the TD-DFT (i.e. the gas phase geometry subject to a PCM (CH_2Cl_2) single-point calculation). The charge and spin density on each porphyrin subunit are almost equal, as depicted for ***I*-P6$^{+\bullet}$** in Figure S15. The geometry difference plots in main text Figure 11 were calculated by comparing the length of each bond in the (gas phase) radical cation geometry to the identical bond in the (gas phase) neutral geometry.

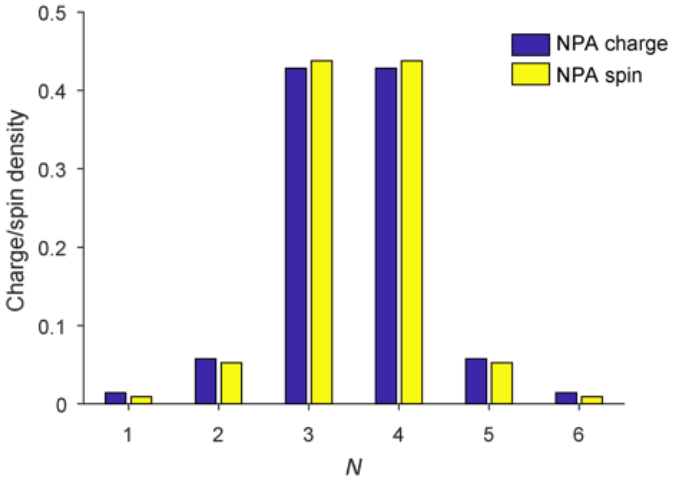

Figure S15. Comparison of per-porphyrin charge and spin densities calculated by the NPA method for ***I*-P6$^{+\bullet}$**. The level of theory was LC-ωPBE/6-31G* (ω = 0.2).

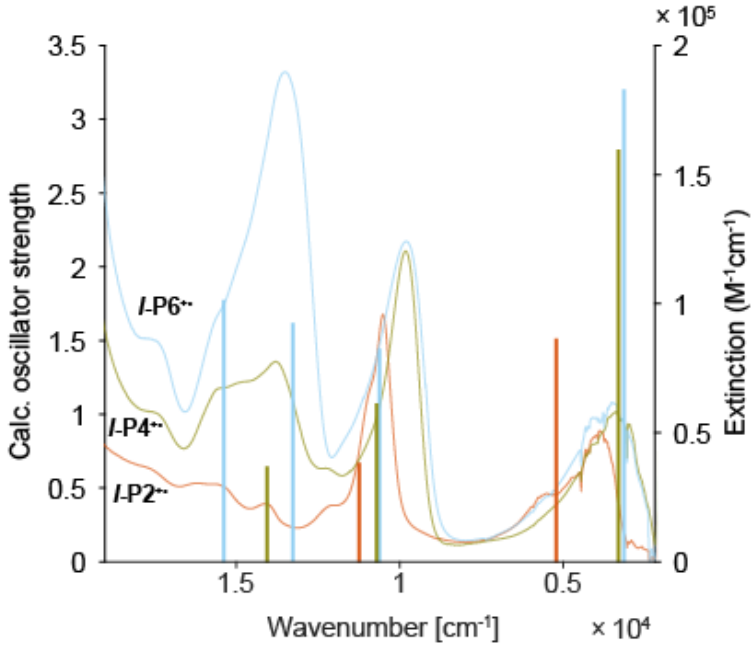

Figure S16. Calculated (sticks) vs. experimental Vis-NIR spectra for ***l*-P2**$^{+\bullet}$ (red), ***l*-P4**$^{+\bullet}$ (gold) and ***l*-P6**$^{+\bullet}$ (blue). Level of theory: LC-ωPBE/6-31G* with a CH_2Cl_2 PCM solvent model.

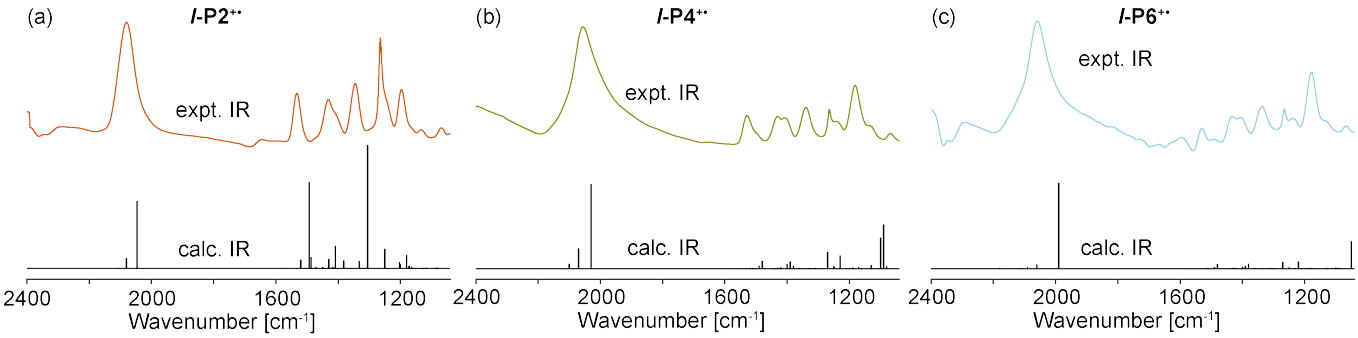

Figure S17. Calculated and experimental IR and Raman spectra for (a) ***l*-P2**$^{+\bullet}$, (b) ***l*-P4**$^{+\bullet}$, (c) ***l*-P6**$^{+\bullet}$. The level of theory for the IR spectra was LC-ωPBE/6-31G*.

MPM simulations

As described in the main text, we used the multistate parabolic model (MPM) described by Rathore and coworkers to describe charge delocalization in our porphyrin oligomers.[20] The MPM Hamiltonian describes a series a parabola (λx^2) coupled by some parameter H_{ab}:

$$\boldsymbol{H} = \begin{bmatrix} \lambda x^2 & H_{ab} & 0 & 0 \\ H_{ab} & \lambda(-x+1)^2 & H_{ab} & 0 \\ 0 & H_{ab} & \lambda(-x+2)^2 & H_{ab} \\ 0 & 0 & H_{ab} & \lambda(-x+3)^2 \end{bmatrix}$$

Division by λ gives a model with a single parameter, H_{ab}/λ.

$$\frac{\boldsymbol{H}}{\lambda} = \begin{bmatrix} x^2 & H_{ab}/\lambda & 0 & 0 \\ H_{ab}/\lambda & (-x+1)^2 & H_{ab}/\lambda & 0 \\ 0 & H_{ab}/\lambda & (-x+2)^2 & H_{ab}/\lambda \\ 0 & 0 & H_{ab}/\lambda & (-x+3)^2 \end{bmatrix}$$

Diagonalizing the Hamiltonian gives the energies of the coupled states (***G***) and the coefficients describing the contribution of each parabola to each state, at a given coordinate *x* (as the columns of Ψ):

$$\boldsymbol{G}/\lambda = \Psi^{-1}\left(\frac{\boldsymbol{H}}{\lambda}\right)\Psi$$

The MPM can be easily extended to account for different parabola energies on different sites (e.g. to capture end group effects).[20,21] A non-quadratic form of the diagonal element has been shown to afford an improved description of higher excited states and long-range delocalization (termed the multistate model, MSM).[22] Addition of coupling between the first and last diagonal elements, and a reformulation of the coordinate x as a radial coordinate, permits the description of cyclic oligomers.[23] Full details can be found in the original publications.[20–24]

The energy difference between the ground and first excited states, $\Delta G/\lambda$, taken at the minimum on the ground sate potential energy surface, should be proportional to the energy of the lowest electronic absorption band in the NIR spectrum. We thus parameterized our coupling parameter, H_{ab}/λ, by systemically varying it to reproduce the trend in the experimental P_1 band. We found that H_{ab}/λ between 1.0 and 1.4 reproduced the experimental trend (shown for $H_{ab}/\lambda = 1.2$ in Figure S18).

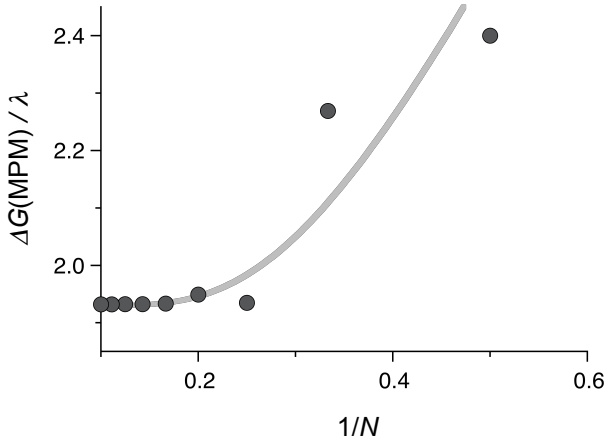

Figure S18. MPM simulation of the energy of the P_1 band as a function of chain length calculated using H = 1.2 λ. The gray line is a fit to the Meier equation [main text footnote 37] as a guide to the eye.

At low values of H_{ab}/λ, the first excited state energy surface simulated using the MPM exhibits some oscillatory structure (Figure S1). This leads to a pronounced odd-even effect in $\Delta G/\lambda$ for shorter oligomers, since the ground state minimum coincides with an excited state maximum for ***l*-P3**, and with an excited state minimum for ***l*-P2** and ***l*-P4**. The parameterization of H_{ab}/λ was therefore necessarily empirical: the primary goal was to reproduce the experimental saturation of $\Delta G/\lambda$ at N = 4.

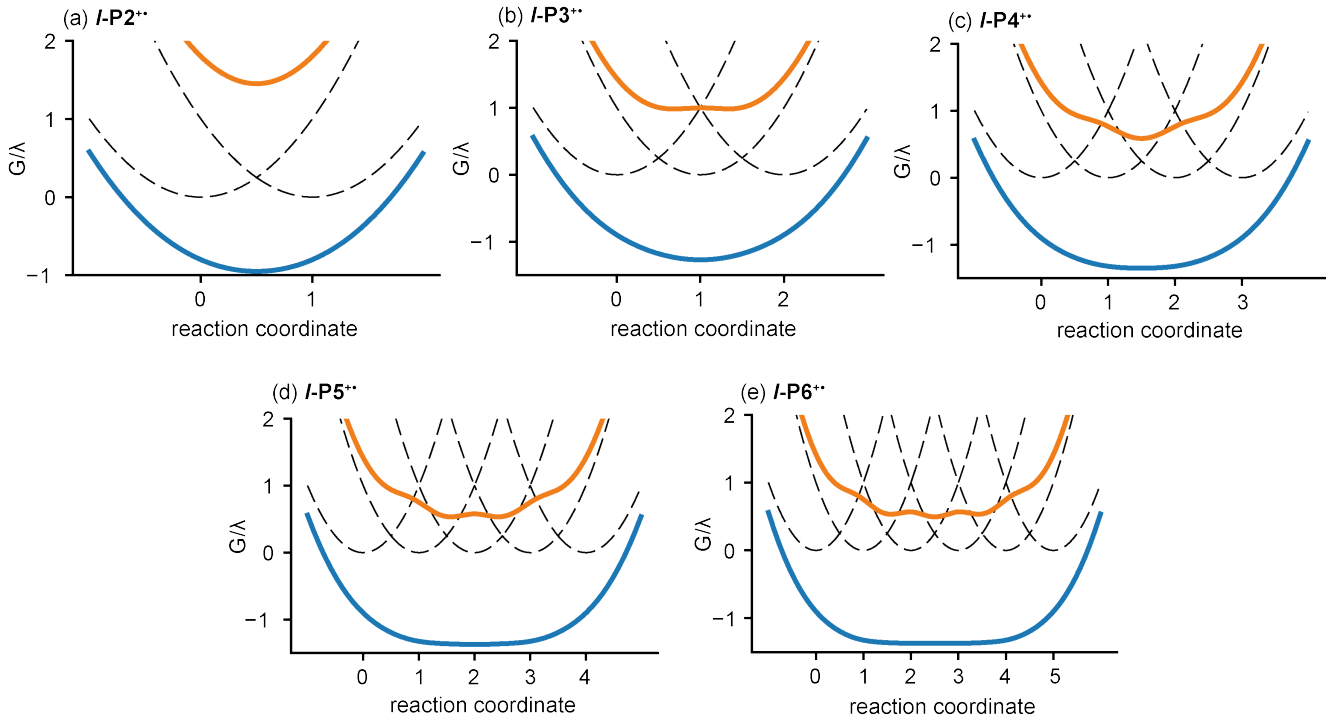

Figure S19. MPM simulations (H = 1.2λ) for ***l*-P2**$^{+\bullet}$ to ***l*-P6**$^{+\bullet}$, showing oscillations in the first excited state potential energy surface (orange). For ***l*-P3**$^{+\bullet}$ and ***l*-P5**$^{+\bullet}$ the position of the minimum in the ground state (blue) corresponds to a local maximum in the excited state; for even oligomers the ground state minimum corresponds to an excited state minimum.[37]

We also attempted to fit the experimental P_1 band energies using the MSM, but this model exhibited the same odd-even effect (Figure S20) in the optimum parameter space, determined by a systematic search.

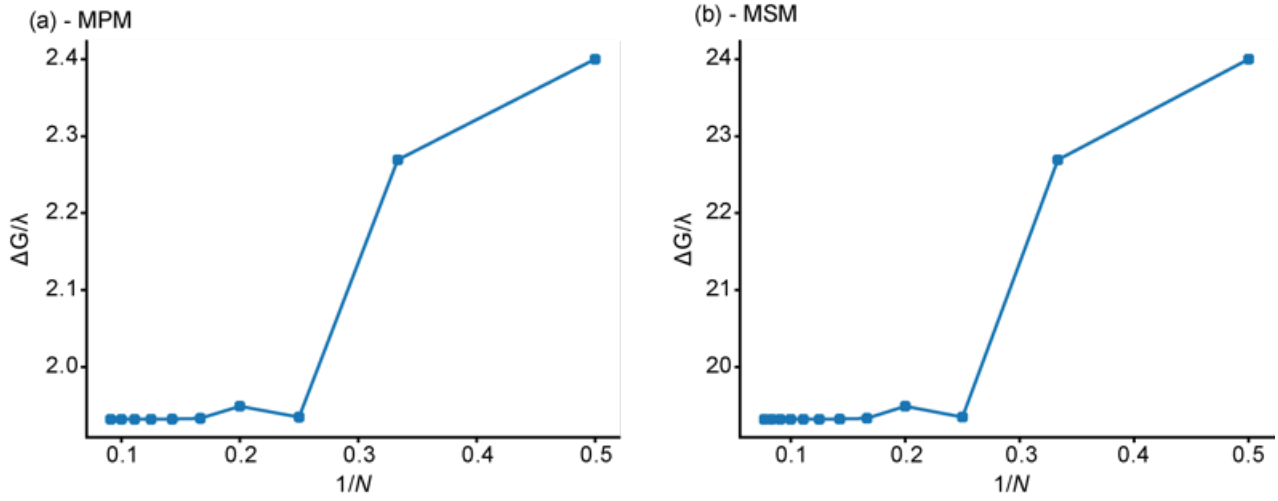

Figure S20. Simulated P_1 band energies from (a) MPM (H = 1.2λ) and (b) MSM (H = 1.2; λ = 1, λ_s = 30) simulations.

The ground state potential energy from the MPM describes the oxidation potential of the oligomer. With increasing oligomer length, the MPM predicts that the first oxidation potential saturates at around N = 4, and this saturation is quite insensitive to the value of H/λ within the range 1.0 to 1.4 (Figure S21a). Experimental square wave voltammetry (CH_2Cl_2 / 0.1 M TBAP, glassy carbon working electrode, platinum wire counter electrode, Ag/AgCl quasi-reference electrode, internally referenced to Fc/Fc^+) appears to approximate the predicted trend (Figures S21b and S16).

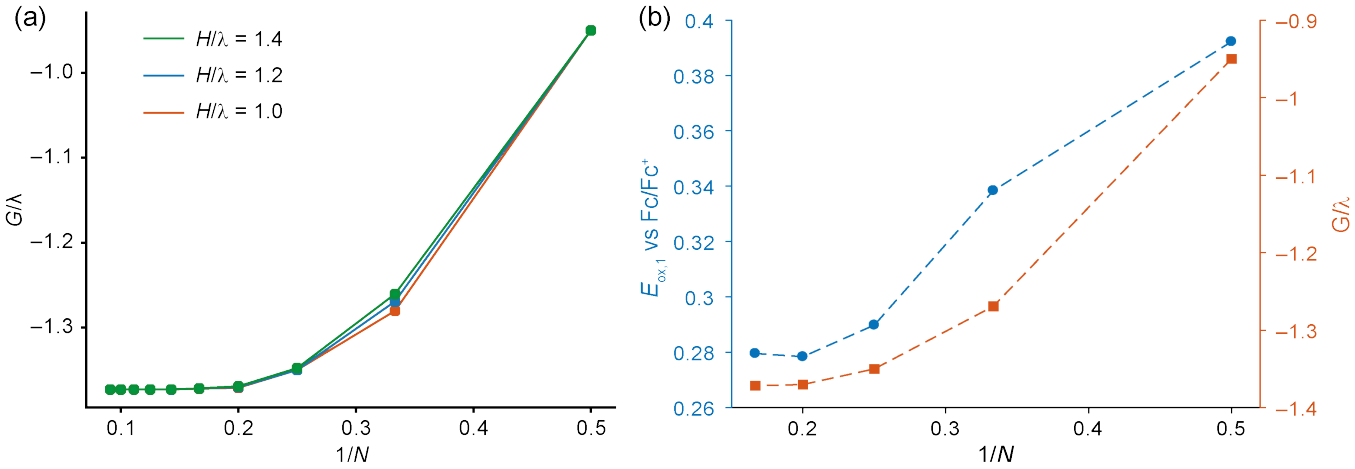

Figure S21. (a) Simulated first oxidation potentials for porphyrin oligomers from the MPM, with various choices for H/λ; (b) comparison of simulated (red, $H/\lambda = 1.2$) and experimental (blue, square wave voltammetry, CH_2Cl_2/0.1 M Bu_4NPF_6) first oxidation potentials for porphyrin oligomers. The experimental potentials are referenced to internal Fc/Fc^+ and are determined by Gaussian fitting of the experimental voltammogram.

References

(1) Grozema, F. C.; Houarner-Rassin, C.; Prins, P.; Siebbeles, L. D. A.; Anderson, H. L. *J. Am. Chem. Soc.* **2007**, *129*, 13370–13371.

(2) Tait, C. E.; Neuhaus, P.; Peeks, M. D.; Anderson, H. L.; Timmel, C. R. *J. Am. Chem. Soc.* **2015**, *137*, 8284–8293.

(3) Neuhaus, P.; Cnossen, A.; Gong, J. Q.; Herz, L. M.; Anderson, H. L. *Angew. Chem. Int. Ed.* **2015**, *54*, 7344–7348.

(4) Yu, F.; Pecoraro, V. L. *Polyhedron* **2013**, *64*, 99–105.

(5) Krejčik, M.; Daněk, M.; Hartl, F. *J. Electroanal. Chem. Interfacial Electrochem.* **1991**, *317*, 179–187.

(6) Peeks, M. D.; Claridge, T. D. W.; Anderson, H. L. *Nature* **2017**, *541*, 200–203.

(7) Jaumot, J.; Gargallo, R.; de Juan, A.; Tauler, R. *Chemom. Intell. Lab. Syst.* **2005**, *76*, 101–110.

(8) Jaumot, J.; de Juan, A.; Tauler, R. *Chemom. Intell. Lab. Syst.* **2015**, *140*, 1–12.

(9) Stoll, S.; Schweiger, A. *J. Magn. Reson.* **2006**, *178*, 42–55.

(10) Frisch, M. J.; Trucks, G. W.; Schlegel, H. B.; Scuseria, G. E.; Robb, M. A.; Cheeseman, J. R.; Scalmani, G.; Barone, V.; Mennucci, B.; Petersson, G. A.; Nakatsuji, H.; Caricato, M.; Li, X.; Hratchian, H. P.; Izmaylov, A. F.; Bloino, J.; Zheng, G.; Sonnenberg, J. L.; Hada, M.; Ehara, M.; Toyota, K.; Fukuda, R.; Hasegawa, J.; Ishida, M.; Nakajima, T.; Honda, Y.; Kitao, O.; Nakai, H.; Vreven, T.; Montgomery Jr., J. A.; Peralta, J. E.; Ogliaro, F.; Bearpark, M.; Heyd, J. J.; Brothers, E.; Kudin, K. N.; Staroverov, V. N.; Kobayashi, R.; Normand, J.; Raghavachari, K.; Rendell, A.; Burant, J. C.; Iyengar, S. S.; Tomasi, J.; Cossi, M.; Rega, N.; Millam, J. M.; Klene, M.; Knox, J. E.; Cross, J. B.; Bakken, V.; Adamo, C.; Jaramillo, J.; Gomperts, R.; Stratmann, R. E.; Yazyev, O.; Austin, A. J.; Cammi, R.; Pomelli, C.; Ochterski, J. W.; Martin, R. L.; Morokuma, K.; Zakrzewski, V. G.; Voth, G. A.; Salvador, P.; Dannenberg, J. J.; Dapprich, S.; Daniels, A. D.; Farkas, Ö.; Foresman, J. B.; Ortiz, J. V; Cioslowski, J.; Fox, D. J. Gaussian Inc.: Wallingford CT 2009.

(11) Ditchfield, R.; Hehre, W. J.; Pople, J. A. *J. Chem. Phys.* **1971**, *54*, 724–728.

(12) Hehre, W. J.; Ditchfield, R.; Pople, J. A. *J. Chem. Phys.* **1972**, *56*, 2257–2261.

(13) Hariharan, P. C.; Pople, J. A. *Theor. Chim. Acta* **1973**, *28*, 213–222.

(14) Rassolov, V. A.; Pople, J. A.; Ratner, M. A.; Windus, T. L. *J. Chem. Phys.* **1998**, *109*, 1223–1229.
(15) Becke, A. D. *J. Chem. Phys.* **1993**, *98*, 5648.
(16) Chai, J.-D.; Head-Gordon, M. *Phys. Chem. Chem. Phys.* **2008**, *10*, 6615–6620.
(17) Vydrov, O. A.; Scuseria, G. E. *J. Chem. Phys.* **2006**, *125*, 234109.
(18) Therien, M. J.; Angiolillo, P. J.; Rawson, J. *Proc. Natl. Acad. Sci.* **2015**, *112*, 13779–13783.
(19) Johnson, R. D. I. *NIST Computational Chemistry Comparison and Benchmark Database*, 18th ed.; Johnson, R. D., Ed.; 2016.
(20) Talipov, M. R.; Boddeda, A.; Timerghazin, Q. K.; Rathore, R. *J. Phys. Chem. C* **2014**, *118*, 21400–21408.
(21) Wang, D.; Talipov, M. R.; Ivanov, M. V.; Rathore, R. *J. Am. Chem. Soc.* **2016**, *138*, 16337–16344.
(22) Talipov, M. R.; Ivanov, M. V.; Rathore, R. *J. Phys. Chem. C* **2016**, *120*, 6402–6408.
(23) Talipov, M. R.; Jasti, R.; Rathore, R. *J. Am. Chem. Soc.* **2015**, *137*, 14999–15006.
(24) Ivanov, M. V.; Talipov, M. R.; Boddeda, A.; Abdelwahed, S. H.; Rathore, R. *J. Phys. Chem. C* **2017**, *121*, 1552–1561.